Journal of Quantitative Spectroscopy & Radiative Transfer 213 (2018) 95–106

Contents lists available at ScienceDirect

Journal of Quantitative Spectroscopy & Radiative Transfer

journal homepage: www.elsevier.com/locate/jqsrt

A plane wave model for direct simulation of reflection and transmission by discretely inhomogeneous plane parallel media

Daniel Mackowski*, Bahareh Ramezanpour

Department of Mechanical Engineering, Auburn University, Auburn, AL 36849, USA

ARTICLE INFO

Article history:
Received 4 October 2017
Revised 3 February 2018
Accepted 3 February 2018
Available online 16 February 2018

ABSTRACT

A formulation is developed for numerically solving the frequency domain Maxwell's equations in plane parallel layers of inhomogeneous media. As was done in a recent work [1], the plane parallel layer is modeled as an infinite square lattice of $W \times W \times H$ unit cells, with W being a sample width of the layer and H the layer thickness. As opposed to the 3D volume integral/discrete dipole formulation, the derivation begins with a Fourier expansion of the electric field amplitude in the lateral plane, and leads to a coupled system of 1D ordinary differential equations in the depth direction of the layer. A 1D dyadic Green's function is derived for this system and used to construct a set of coupled 1D integral equations for the field expansion coefficients. The resulting mathematical formulation is considerably simpler and more compact than that derived, for the same system, using the discrete dipole approximation applied to the periodic plane lattice. Furthermore, the fundamental property variable appearing in the formulation is the Fourier transformed complex permittivity distribution in the unit cell, and the method obviates any need to define or calculate a dipole polarizability. Although designed primarily for random media calculations, the method is also capable of predicting the single scattering properties of individual particles; comparisons are presented to demonstrate that the method can accurately reproduce, at scattering angles not too close to 90°, the polarimetric scattering properties of single and multiple spheres. The derivation of the dyadic Green's function allows for an analytical preconditioning of the equations, and it is shown that this can result in significantly accelerated solution times when applied to densely-packed systems of particles. Calculation results demonstrate that the method, when applied to inhomogeneous media, can predict coherent backscattering and polarization opposition effects.

1. Introduction

A recent article from our group discussed the formulation of DDA[1] to the prediction of EM plane wave scattering by a discretely and randomly inhomogeneous, plane parallel medium; the motivation for this being the development of direct simulation methods for predicting polarimetric reflection from particle layers, inhomogeneous films, regolith, and the like [1]. Direct simulation methods, in the present context, rely on some probabilistic, Monte Carlo-type procedure to generate sample configurations of the random medium within a prescribed unit cell volume. The volume must be sufficiently large to capture the statistics of the medium, and the spatial resolution obviously must be on par with the smallest controlling length scale characterizing the EM transport process; the latter is typically the wavelength but can be smaller, e.g., photonic applications.

The unit cell can form the building block for a mathematically–convenient idealization of the real, infinite layer as a periodic array of identical unit cells; for such systems – and plane wave incidence – a straightforward and computationally tractable extension of the DD formulation is possible. Observable polarimetric properties of the layer, such as the 4×4 reflection matrix elements, would be obtained from the averaging of solutions to multiply sampled configurations. A basic, implied assumption is that, given a sufficiently wide unit cell, the configuration–averaged scattered field for the periodic PP layer would be indistinguishable from that calculated (hypothetically) for a completely random layer, i.e., that having an infinite cell width. The testing of this assumption would need to be part of any numerical experiment employing the method.

The algorithms used to sample configurations produce maps of refractive index (or, equivalently, dipole polarizability) within the unit cell, as a function of the three spatial coordinates. In [1], it was demonstrated that the actual DD calculations are more

* Corresponding author.
E-mail address: mackodw@auburn.edu (D. Mackowski).
[1] Acronyms are defined in the appendix.

https://doi.org/10.1016/j.jqsrt.2018.02.003
0022-4073/

efficiently performed in reciprocal space (RS), which is obtained from the 2D DFT of the DD equations in the lateral plane; the lateral coordinates x^i and y^i of the dipole element i become replaced with wavenumber variables k_x^s and k_y^s for reciprocal lattice element s. In particular, the transformed polarizability distribution in k_x, k_y, and z variables, contained in a $2\mathrm{k}_R \times 2\mathrm{k}_R \times H$ unit cell *and* representative of the infinite medium, becomes the fundamental *a-priori* information used in the DD algorithm. A very limited set of calculations in [1] showed that the reciprocal space unit cell width could be truncated at around $\mathrm{k}_R \sim 2-4$ with unobservable effect on the prediction results; this value is significantly less than the maximum RS unit cell width of $\mathrm{k}_{max} = \pi/d \sim 10-20$, where d is the dimensionless dipole spacing. There are other advantages of a RS formulation; most notably that the subset of the k_x, k_y variables – those belonging to the propagating wavevectors having $|\mathrm{k}_x|^2 + |\mathrm{k}_y|^2 < 1$ – correspond to the primitive coordinates of the polarimetric observables, i.e., angular position. The DD equations also naturally adapt to a preconditioning scheme in RS.

This duality in the spaces used in the direct simulation process – direct space for the configuration samples, RS for the computations – can make one think about the DD formulation for the plane parallel system and its derivation. This derivation starts with the transformation of the 3D vector Helmholtz equation for the electric field amplitude into a volume integral equation (VIE); the DD model represents the discretized approximation to this VIE. This model is then reformulated for the periodic plane parallel lattice, per the procedure originally developed by Draine and Flatau [2]. Finally, the periodic formulation is DFT'd in the lateral plane to produce the RS model.

It would appear perfectly valid to put the last step in this process in the first position. The DFT of the 3D Helmholtz equation would produce a system of 1D ordinary differential equations. A Green's function for this system could be identified and used to construct a system of 1D VIEs. And this system could be discretized into a numerical approximation. A hunch, in starting this work, was that this approach could simplify and/or obviate many of the issues associated with the DD plane parallel formulation, particularly in the formulas for the polarizability and dyadic Green's function for the periodic lattice.

Presented in this work is a formulation that follows this line of thought. The basic idea does not seem that complicated, and if it could actually work one might expect that it would have been in common use by now among the scattering/remote sensing scientific community. Surprisingly to us, we were unable to find any electromagnetic scattering reference that arrives at the same general working model as that derived here. The scope of the search was mainly limited to the EM propagation field, and did not branch out into solid state physics, acoustic, and other fields sharing the same mathematical landscape. Major works on the application of volume integral methods to EM wave propagation in periodic and random media abound, yet from what we can tell they all involve an initial direct space representation of the dyadic Green's function. This DGF can be transformed in subsequent operations into RS, yet it begins in DS.

The paper begins by developing RS 1D volume integral formulation, which is referred to as the plane wave plane parallel (PWPP) model; this acronym is chosen because the basic mathematical element in the model will be a plane wave, as opposed to a radiating dipole in DD. A discretized model of the 1D VIEs are then constructed and implemented in a FORTRAN-90+MPI code. Test calculation results, involving the prediction of directional polarized scattering by single or multiple spheres, are performed and compared to known benchmarks. Finally, the method is applied to random media.

2. Formulation

2.1. Helmholtz equation for the periodic plane parallel system

A dimensionless formulation will be adopted in which all lengths are scaled by $1/\mathrm{k}_0$, with $\mathrm{k}_0 = 2\pi/\lambda_0$ is the free space wavenumber and λ_0 the vacuum wavelength of the incident wave. Let $z = 0$ and $z = H$ denote the planes where the inhomogeneous medium starts and stops. The halfspace $z < 0$, referred to as region 0, has unit permittivity and within which is imposed an upward propagating, unit amplitude, and linearly polarized plane wave with wavevector $\mathbf{k}^0$. The halfspace $z > H$ (region H) has permittivity ϵ_H, which may be complex.

The vector partial differential equation to be solved, assuming nonmagnetic media and an $\exp(-i\omega t)$ time harmonic factor, is the vector Helmholtz equation for the electric field amplitude,

$$-\nabla \times \nabla \times \mathbf{E}(\mathbf{r}) + \epsilon(\mathbf{r})\mathbf{E}(\mathbf{r}) = 0 \tag{1}$$

subject to the constraint (or ultimate computational ceiling) that the permittivity $\epsilon(\mathbf{r})$ is microscopically known only within a finite unit cell of volume W^2H. This work is focussed on situations in which the permittivity of the layer is not a periodic function by design, and the cell width W should be viewed simply as a sample size of the medium. Given this constraint, the modeling objective is to predict, via a direct solution of Eq. (1) using the given $\epsilon(\mathbf{r})$, the polarimetric field reflected and transmitted by a laterally-infinite, plane-parallel layer of the material that has a permittivity distribution statistically identical to the one used to construct $\epsilon(\mathbf{r})$.

Perhaps the least difficult route to this objective is to replace the real, infinite medium with a 2D infinite square lattice of the unit cells. This can be accommodated into the DD model by summing the Green's function over the infinite lattice [1,2]. But consider what is going on when the dipole-based model is recast into a plane parallel role: a fundamental feature of a dipole model is that the dipole source automatically obeys the Sommerfeld far-field condition. There is no need for this condition in a plane parallel problem, for which space is one dimensional in the far-field and the proper asymptotic form of the electric field is a vector transverse plane wave. This is (as it has to be) the far-field form of the periodic DD Green's function, but it takes a discrete Fourier transform in the lateral plane to make it explicit.

What is done here is very simple: the Fourier transform is performed, at the outset, on the governing PDE. The periodic boundary conditions at $x, y = \pm W/2$ are identically satisfied by a Fourier series expansion of the electric field,

$$\mathbf{E}(\mathbf{r}) = \sum_{\mathbf{s}} \mathbf{p}^{\mathbf{s}}(z) e^{i\,\mathbf{k}_\rho^{\mathbf{s}} \cdot \boldsymbol{\rho}} \tag{2}$$

where $\boldsymbol{\rho}$ is the lateral position vector so that $\mathbf{r} = \boldsymbol{\rho} + z\hat{\mathbf{z}}$, $\mathbf{p}^{\mathbf{s}}(z) = p_x^{\mathbf{s}}(z)\,\hat{\mathbf{x}} + p_y^{\mathbf{s}}(z)\,\hat{\mathbf{y}} + p_z^{\mathbf{s}}(z)\,\hat{\mathbf{z}}$ is a vector amplitude for the $\mathbf{s}$ mode wave,

$$\mathbf{k}_\rho^{\mathbf{s}} = \mathbf{k}_\rho^0 + \frac{2\pi\,\mathbf{s}}{W}, \quad \mathbf{s} = s_x\hat{\mathbf{x}} + s_y\hat{\mathbf{y}}, \quad s_x, s_y = 0, \pm 1, \pm 2, \ldots \tag{3}$$

is the 2D reciprocal lattice (RL) vector, which are the eigenvalues of the eigenfunction in Eq. (2), and $\mathbf{k}_\rho^0$ is the projection of the incident direction onto the lateral plane. The orthogonality properties of the eigenfunctions will transform Eq. (1) into a system of vector ODEs for the $\mathbf{p}^{\mathbf{s}}(z)$ vector amplitudes:

$$-\widetilde{\nabla}^{\mathbf{s}} \times \widetilde{\nabla}^{\mathbf{s}} \times \mathbf{p}^{\mathbf{s}}(z) + \sum_{\mathbf{s}'} \widetilde{\epsilon}^{\,\mathbf{s}-\mathbf{s}'}(z)\,\mathbf{p}^{\mathbf{s}'}(z) = 0 \tag{4}$$

in which

$$\widetilde{\nabla}^{\mathbf{s}}\times = \begin{pmatrix} 0 & -d/dz & i\,\mathrm{k}_y^{\mathbf{s}} \\ d/dz & 0 & -i\,\mathrm{k}_x^{\mathbf{s}} \\ -i\,\mathrm{k}_y^{\mathbf{s}} & i\,\mathrm{k}_x^{\mathbf{s}} & 0 \end{pmatrix} \tag{5}$$

and

$$\widetilde{\epsilon}^{\mathbf{s}}(z) = \frac{1}{W^2}\int_{-W/2}^{W/2} dx \int_{-W/2}^{W/2} dy\, \epsilon(\boldsymbol{\rho}, z) e^{-\mathrm{i}\,\mathbf{k}_\rho^{\mathbf{s}}\cdot\boldsymbol{\rho}} \tag{6}$$

Truncation of the expansion in Eq. (2) at some *a-priori* S_R is needed for closure of the equations; counting positive and negative indices this results in $3(2S_R+1)^2$ ODEs in all.

The expansion of the electric field in Eq. (2), and the system of ODEs for the vector amplitude functions in Eq. (4), are basic relations in the PWPP model. The fundamental idea is to represent the field on any lateral plane in the unit cell as an expansion of functions continuous at every point on the plane. There are obvious questions with this approach when applied to piecewise-continuous media, and it would make little sense if the objective was to accurately predict the *spatial* distribution of field strength in the cell.

On the other hand, the method can make a lot of sense when the objective is to model the far-field reflection and transmission characteristics of the layer. The scattered field will be described by a discrete distribution, in $\mathbf{k}_\rho^{\mathbf{s}}$ space, of the $\mathbf{p}^{\mathbf{s}}$ vector amplitudes at the top and the bottom of the layer. The information contained in the propagating spectrum, corresponding to $|\mathbf{k}_\rho^{\mathbf{s}}| < 1$ or $|m_H|$, is the primitive variable of interest to radiative transfer and remote sensing, i.e, the directional, polarimetric reflection and transmission of the layer. In this regard, the truncation criterion on Eq. (2) – that of setting S_R – becomes analogous to a spectral windowing operation: the size of the unit cell in $\mathbf{k}_\rho^{\mathbf{s}}$ space will be large enough when further increases no longer alter the propagating part of the spectrum. It is recognized that this implicitly assumes that the truncation error monotonically decreases: once it flattens out it stays there, and there is no hidden structure of the medium in high-$\mathbf{k}_\rho$ space that would fundamentally alter the polarimetric scattering features of the medium.

The spatial 1D primitive variable characterizing the EM response of the medium becomes the lateral discrete Fourier spectrum of the permittivity. In view of the convolution in Eq. (4) and the truncation on Eq. (2), this spectrum is needed out to $2S_R$ RL modes. Importantly, this will allow the use of large direct space unit cell widths W, in conjunction with Monte Carlo algorithms, to generate realistic configurations of random, plane-parallel media.

A consequence of the periodic model is that reflected and transmitted fields, as predicted, are strictly in the form of a diffraction pattern, i.e., a discrete directional superposition of plane waves. The direction vectors will be given by

$$\hat{\mathbf{x}}\,\sin\theta^{\mathbf{s}}\cos\phi^{\mathbf{s}} + \hat{\mathbf{y}}\,\sin\theta^{\mathbf{s}}\sin\phi^{\mathbf{s}} = \mathbf{k}_\rho^{\mathbf{s}} \tag{7}$$

and the angular width between peaks will be $\Delta\theta \sim 2\pi/W$ for $2\pi/W \ll 1$. The direct space cell width, in this regard, also sets the angular resolution of the predictions – providing that nothing beyond lattice point interpolation is used to calculate the field.

Noted is perhaps the obvious, especially in regard to the previous paragraph: the periodic, unit cell model is somewhat contrived in view of the stated objectives, and a more honest approach would be to replace Eq. (2) with a Fourier integral transform – taken out to $\pm\infty$ in the lateral plane – and go from there. The resulting integrals over $\mathbf{k}_\rho$ space could be approximated via azimuthal degree decomposition and polar quadrature, much like that done in numerical PP RT algorithms [3]; unlike RT the polar coordinate would extend into the evanescent domain, i.e., $\sin\theta$ now goes from 0 to ∞. Perhaps there is some potential in this approach; it could potentially reduce the overall DOF in the numerical model without sacrificing accuracy. The periodic, eigenfunction–based model of Eq. (2), on the other hand, does couple seamlessly to an FFT-based algorithm for solving Eq. (4), and the inefficiency of the $\mathbf{k}_\rho$-space representation is mitigated by the speed of the code.

Aside for the trivial case of a homogeneous medium – for which both $\mathbf{p}^{\mathbf{s}}$ and $\widetilde{\epsilon}^{\,\mathbf{s}}$ are zero for all $\mathbf{s}\neq 0$ – situations in which analytical solutions of Eq. (4) are possible will not be explored. The adopted numerical method will be based upon a Green's function solution to Eq. (4), and will produce a system of equations analogous to that for the DD model. It is noted that a finite difference form of Eq. (4) would not be difficult to devise, and Robin-type boundary conditions – analogous to perfectly absorbing conditions – could be formulated at the $z=0$ and H boundaries. And perhaps there is also some potential to this approach, although it is not likely in view of the rare mention of frequency domain finite difference methods in the scattering literature.

2.2. Dyadic Green's function for the periodic plane parallel system

Following the route used to derive the 3D volume integral equation [4], Eq. (4) is rearranged into the pseudo–inhomogeneous form:

$$\left(-\widetilde{\nabla}^{\mathbf{s}}\times\widetilde{\nabla}^{\mathbf{s}}\times + \overline{\epsilon}\right)\mathbf{p}^{\mathbf{s}}(z) = -\mathbf{a}^{\mathbf{s}}(z;\overline{\epsilon}) \tag{8}$$

where the source $\mathbf{a}^{\mathbf{s}}(z;\overline{\epsilon})$ is

$$\mathbf{a}^{\mathbf{s}}(z;\overline{\epsilon}) = \sum_{\mathbf{s}'}\left(\widetilde{\epsilon}^{\,\mathbf{s}-\mathbf{s}'}(z) - \overline{\epsilon}\,\delta_{\mathbf{s}-\mathbf{s}'}\right)\mathbf{p}^{\mathbf{s}'}(z) \tag{9}$$

with $\delta_{\mathbf{s}-\mathbf{s}'}$ being the Kronecker delta function. The constant permittivity $\overline{\epsilon}$ appearing in Eq. (8), referred to as the DGF permittivity, is currently undefined; in the traditional VIE derivation it would be unity and would lead to a formulation based on the free space Green's function. It obviously has no effect on the exact solution of Eq. (8) for a prescribed permittivity distribution and incident field. However, it can have a substantial and very useful effect on the computational effort required to obtain a numerical solution to Eq. (8).

The equation for the DGF replaces the source in Eq. (8) with the Dirac delta function $\delta(z-z')$ times the unit dyad, with $0<z'<H$, and results in a 3×3 system of second order ODEs for $\mathbf{G}^{\mathbf{s}}(z,z';\overline{\epsilon})$ at each RL mode $\mathbf{s}$. The complexity of the problem can be reduced by first performing a $\mathbf{s}$-dependent rotation about the z axis, so that the new x and y coordinates become parallel and perpendicular to the meridional plane formed by $\hat{\mathbf{z}}$ and $\mathbf{k}_\rho^{\mathbf{s}}$; these new coordinates will be denoted as x' and y' and the rotated DGF as $\widetilde{\mathbf{G}}$. The rotation operation is

$$\widetilde{\mathbf{G}}^{\mathbf{s}}(z,z';\overline{\epsilon}) = \begin{pmatrix} \widetilde{G}^{\mathbf{s}}_{x',x'} & 0 & \widetilde{G}^{\mathbf{s}}_{x',z} \\ 0 & \widetilde{G}^{\mathbf{s}}_{y',y'} & 0 \\ \widetilde{G}^{\mathbf{s}}_{z,x'} & 0 & \widetilde{G}^{\mathbf{s}}_{z,z} \end{pmatrix} = R^{\mathbf{s}}\cdot\mathbf{G}^{\mathbf{s}}(z,z';\overline{\epsilon})\cdot R^{\mathbf{s}} \tag{10}$$

where

$$R^{\mathbf{s}} = \begin{pmatrix} \cos\phi^{\mathbf{s}} & \sin\phi^{\mathbf{s}} & 0 \\ \sin\phi^{\mathbf{s}} & -\cos\phi^{\mathbf{s}} & 0 \\ 0 & 0 & 1 \end{pmatrix} \tag{11}$$

and

$$e^{i\phi^{\mathbf{s}}} = \frac{\mathrm{k}_x^{\mathbf{s}} + \mathrm{i}\,\mathrm{k}_y^{\mathbf{s}}}{\mathrm{k}_\rho^{\mathbf{s}}}, \quad \mathrm{k}_\rho^{\mathbf{s}} = \left|\mathbf{k}_\rho^{\mathbf{s}}\right| \tag{12}$$

In the limit of $\left|\mathbf{k}_\rho^{\mathbf{s}}\right| \to 0$, $\cos\phi\to 1$ and $\sin\phi\to 0$. Since R is unitary, the inverse transformation is the same as Eq. (10), with $\mathbf{G}$ and $\widetilde{\mathbf{G}}$ interchanged.

The differential equation for the DGF, in the rotated coordinates, appears as

$$\mathbf{L}^{\mathbf{s}}(z;\overline{\epsilon})\cdot\widetilde{\mathbf{G}}^{\mathbf{s}}(z,z';\overline{\epsilon}) = -\mathbf{I}\,\delta(z-z'), \quad 0\le z\le H, \quad 0<z'<H \tag{13}$$

with

$$\mathbf{L}^{\mathbf{s}}(z;\overline{\epsilon}) = \begin{pmatrix} d^2/dz^2 + \overline{\mathrm{m}}^2 & 0 & -\mathrm{i}\mathrm{k}_\rho^{\mathbf{s}}\, d/dz \\ 0 & d^2/dz^2 + (\overline{\mathrm{m}}\,\mathrm{k}_z^{\mathbf{s}})^2 & 0 \\ -\mathrm{i}\,\mathrm{k}_\rho^{\mathbf{s}}\, d/dz & 0 & (\overline{\mathrm{m}}\,\mathrm{k}_z^{\mathbf{s}})^2 \end{pmatrix} \tag{14}$$

in which $\overline{\mathrm{m}} = \sqrt{\overline{\epsilon}}$ is the DGF refractive index and

$$\overline{\mathrm{m}}\,\mathrm{k}_z^{\mathbf{s}} = \sqrt{\overline{\mathrm{m}}^2 - \mathrm{k}_\rho^{\mathbf{s}2}} \tag{15}$$

The root in Eq. (15) is chosen so that $0 \le \mathrm{Arg}\,[\overline{\mathrm{m}}\,\mathrm{k}_z^{\mathbf{s}}] < \pi$.

Separate solutions, in the form of a superposition of upward and downward–directed plane waves, can be obtained in the internal regions $0 \le z < z'$ and $z' < z \le H$ for each column vector of Eq. (13). A homogenous form of Eq. (13) (i.e., absent the delta function) can also be written for the external regions $z \le 0$ and $z \ge H$ by replacing $\overline{\epsilon}$ with either 1 or ϵ_H; the fields in these regions will appear as plane waves directed away from the slab. At the boundaries of the system ($z = 0$ and H) the tangential components of $\widetilde{\mathbf{G}}$ and its curl will match those of the external fields. The tangential components of $\widetilde{\mathbf{G}}$ can also be matched as $z \to z'$, and a final condition is obtained by dotting Eq. (13) with $\hat{\mathbf{z}}$, employing Green's identities, integrating the result over z from $z' - \Delta z$ to $z' + \Delta z$, and taking the limit as $\Delta z \to 0$; this last part will produce the sole singularity in the DGF, that being a Dirac delta function part to the $\hat{\mathbf{z}}\hat{\mathbf{z}}$ element.

The end result can be put in a relatively compact form:

$$\widetilde{\mathbf{G}}^{\mathbf{s}}(z,z') = \widetilde{\mathbf{G}}^{\mathbf{s}}_{reg}(z,z') - \frac{1}{\overline{\epsilon}}\,\delta(z-z')\,\hat{\mathbf{z}}\hat{\mathbf{z}} \tag{16}$$

$$\widetilde{\mathbf{G}}^{\mathbf{s}}_{reg}(z,z') = H(z-z')\widetilde{\mathbf{G}}^{\mathbf{s}}_{+,reg}(z,z') + H(z'-z)\widetilde{\mathbf{G}}^{\mathbf{s}}_{-,reg}(z,z') \tag{17}$$

$$\begin{aligned}\widetilde{\mathbf{G}}^{\mathbf{s}}_{+,reg}(z,z') &= C^{\mathbf{s}}_{\parallel}\boldsymbol{\Psi}^{\mathbf{s}}_{+\parallel,H}(H-z) \otimes \boldsymbol{\Psi}^{\mathbf{s}}_{+\parallel,0}(z') \\ &\quad + C^{\mathbf{s}}_{\perp}\boldsymbol{\Psi}^{\mathbf{s}}_{\perp,H}(H-z) \otimes \boldsymbol{\Psi}^{\mathbf{s}}_{\perp,0}(z')\end{aligned} \tag{18}$$

$$\begin{aligned}\widetilde{\mathbf{G}}^{\mathbf{s}}_{-,reg}(z,z') &= C^{\mathbf{s}}_{\parallel}\boldsymbol{\Psi}^{\mathbf{s}}_{-\parallel,0}(z) \otimes \boldsymbol{\Psi}^{\mathbf{s}}_{-\parallel,H}(H-z') \\ &\quad + C^{\mathbf{s}}_{\perp}\boldsymbol{\Psi}^{\mathbf{s}}_{\perp,0}(z) \otimes \boldsymbol{\Psi}^{\mathbf{s}}_{\perp,H}(H-z')\end{aligned} \tag{19}$$

$$\boldsymbol{\Psi}^{\mathbf{s}}_{\sigma\parallel,B}(z) = \psi^{\mathbf{s}}_{\parallel,B}(z)\,\hat{\mathbf{x}}' - \frac{\sigma\,\mathrm{i}\sqrt{1-\mathrm{k}_z^{\mathbf{s}2}}}{\overline{\mathrm{m}}\,\mathrm{k}_z^{\mathbf{s}2}}\,\psi'^{\mathbf{s}}_{\parallel,B}(z)\,\hat{\mathbf{z}} \tag{20}$$

$$\boldsymbol{\Psi}^{\mathbf{s}}_{\perp,B}(z) = \mathrm{i}\,\psi^{\mathbf{s}}_{\perp,B}(z)\,\hat{\mathbf{y}}' \tag{21}$$

$$\psi^{\mathbf{s}}_{\parallel,B}(z) = \mathrm{i}\,\overline{\mathrm{m}}\,\mathrm{k}^{\mathbf{s}}_{z,B}\cos(\overline{\mathrm{m}}\mathrm{k}^{\mathbf{s}}_z z) + \mathrm{m}_B\mathrm{k}^{\mathbf{s}}_z\sin(\overline{\mathrm{m}}\mathrm{k}^{\mathbf{s}}_z z) \tag{22}$$

$$\psi^{\mathbf{s}}_{\perp,B}(z) = \mathrm{i}\,\overline{\mathrm{m}}\,\mathrm{k}^{\mathbf{s}}_z\cos(\overline{\mathrm{m}}\mathrm{k}^{\mathbf{s}}_z z) + \mathrm{m}_B\mathrm{k}^{\mathbf{s}}_{z,B}\sin(\overline{\mathrm{m}}\mathrm{k}^{\mathbf{s}}_z z) \tag{23}$$

$$C^{\mathbf{s}}_{\parallel} = \frac{\mathrm{k}^{\mathbf{s}}_z}{\overline{\mathrm{m}}(\mathrm{i}\,\overline{\mathrm{m}}\,\mathrm{k}^{\mathbf{s}}_z(\mathrm{k}^{\mathbf{s}}_{z,H} + \mathrm{m}_H\mathrm{k}^{\mathbf{s}}_{z,0})\cos(\overline{\mathrm{m}}\mathrm{k}^{\mathbf{s}}_z H) + (\overline{\mathrm{m}}^2\mathrm{k}^{\mathbf{s}}_{z,0}\mathrm{k}^{\mathbf{s}}_{z,H} + \mathrm{m}_H\mathrm{k}^{\mathbf{s}2}_z)\sin(\overline{\mathrm{m}}\mathrm{k}^{\mathbf{s}}_z H))} \tag{24}$$

$$C^{\mathbf{s}}_{\perp} = \frac{1}{\mathrm{i}\,\overline{\mathrm{m}}^2\mathrm{k}^{\mathbf{s}2}_z(\mathrm{k}^{\mathbf{s}}_{z,0} + \mathrm{m}_H\mathrm{k}^{\mathbf{s}}_{z,H})\cos(\overline{\mathrm{m}}\mathrm{k}^{\mathbf{s}}_z H) + \overline{\mathrm{m}}\mathrm{k}^{\mathbf{s}}_z(\overline{\mathrm{m}}^2\mathrm{k}^{\mathbf{s}2}_z + \mathrm{m}_H\mathrm{k}^{\mathbf{s}}_{z,0}\mathrm{k}^{\mathbf{s}}_{z,H})\sin(\overline{\mathrm{m}}\mathrm{k}^{\mathbf{s}}_z H)} \tag{25}$$

In the above, $H(z) = 0, 1$ for $z <, > 0$ is the Heaviside step function, B denotes 0 or H, $\sigma = \pm 1$, $\otimes$ denotes outer product, and the prime denotes differentiation with respect to the argument. The z component of the wavevectors in the 0 and H regions are given by Snell's law:

$$\mathrm{k}^{\mathbf{s}}_\rho = \sqrt{1 - \mathrm{k}^{\mathbf{s}2}_{z,0}} = \mathrm{m}_H\sqrt{1 - \mathrm{k}^{\mathbf{s}2}_{z,H}} \tag{26}$$

In the free space condition, corresponding to $\epsilon_H = \overline{\epsilon} = 1$, the DGF reduces to a very simple form involving the dyadic products of vector transverse plane waves:

$$\widetilde{\mathbf{G}}^{\mathbf{s}}(z,z')\Big|_{FS} = \frac{\mathrm{i}}{2\mathrm{k}^{\mathbf{s}}_z}\,e^{\mathrm{i}\,\mathrm{k}^{\mathbf{s}}_z|z-z'|}\left[\mathbf{e}^{\mathbf{s}}_{\parallel} \otimes \mathbf{e}^{\mathbf{s}}_{\parallel} + \hat{\mathbf{y}}' \otimes \hat{\mathbf{y}}'\right] - \delta(z-z')\,\hat{\mathbf{z}} \otimes \hat{\mathbf{z}} \tag{27}$$

$$\mathbf{e}^{\mathbf{s}}_{\parallel} = \mathrm{k}^{\mathbf{s}}_z\hat{\mathbf{x}}' - \sigma\sqrt{1-\mathrm{k}^{\mathbf{s}2}_z}\,\hat{\mathbf{z}} \tag{28}$$

with $\sigma = \mathrm{sign}\,(z - z')$. When $|z - z'| > 0$, the free space formula for the DGF in Eq. (27) is equivalent to that derived (via a lengthier process) from a DFT of the dyadic Green's function appearing in the 2D periodic DD model.

As is the case with any Green's function, the PWPP DGF describes the excitation at one point in the medium due to a source at another point. The nature of this excitation will be determined, to a large extent, by the magnitude of the RL vector $\mathrm{k}^{\mathbf{s}}_\rho$. In particular, the evanescent RL modes corresponding to $|\mathbf{k}^{\mathbf{s}}_\rho| > |\overline{\mathrm{m}}|$ will result in a decaying exponential dependence of $\widetilde{\mathbf{G}}^{\mathbf{s}}$ with $|z - z'|$, and the rate of decay will increase as $2\pi|\mathbf{s}|/W \gg |\overline{\mathrm{m}}|$.

2.3. Integral equation for the periodic plane parallel system

The integral equation for the complex electric field amplitude appears as

$$\mathbf{p}^{\mathbf{s}}(z) = \Phi^0(z;\overline{\epsilon})\delta_{\mathbf{s}} + \int_0^H dz'\,\mathbf{G}^{\mathbf{s}}(z,z';\overline{\epsilon}) \cdot \mathbf{a}^{\mathbf{s}}(z';\overline{\epsilon}) \tag{29}$$

The incident amplitude $\Phi^0(z;\overline{\epsilon})$ describes the transverse vector plane wave existing inside a homogeneous slab, of thickness H and refractive index $\overline{\mathrm{m}}$, that is bordered by media with refractive indices 1 and m_H and excited by a unit–amplitude plane wave propagating in medium 0 towards the slab; the explicit formula is given in the appendix. Eq. (29) is a straightforward superposition solution to the inhomogeneous Helmholtz equation of Eq. (4) and the inhomogeneous boundary condition due to the incident plane wave: the first term satisfies the homogeneous Helmholtz equation and the inhomogeneous boundary conditions, and the second term satisfies the inhomogeneous equation and the homogeneous boundary conditions of zero incident field.

An equivalent formulation based on the source function is obtained by using Eq. (9) in (29), resulting in

$$\mathbf{a}^{\mathbf{s}}(z) - \sum_{\mathbf{s}'}\hat{\epsilon}^{\,\mathbf{s}-\mathbf{s}'}(z)\int_0^H dz'\,\mathbf{G}^{\mathbf{s}'}(z,z') \cdot \mathbf{a}^{\mathbf{s}'}(z') = \hat{\epsilon}^{\,\mathbf{s}}(z)\,\Phi^0(z) \tag{30}$$

where the quantity $\hat{\epsilon}^{\,\mathbf{s}}(z;\overline{\epsilon})$ is defined as

$$\hat{\epsilon}^{\,\mathbf{s}}(z) = \widetilde{\epsilon}^{\,\mathbf{s}}(z) - \overline{\epsilon}\,\delta_{\mathbf{s}} \tag{31}$$

In the above and what follows the dependency of $\mathbf{a}^{\mathbf{s}}, \Phi^0, \hat{\epsilon}^{\,\mathbf{s}}$ and $\mathbf{G}^{\mathbf{s}}$ on $\overline{\epsilon}$ will be explicitly indicated only when needed. Eq. (30), which describes how the RS spectrum of the electric displacement field evolves in depth z, is the fundamental governing equation of the PWPP model.

Given a permittivity distribution $\hat{\epsilon}^{\,\mathbf{s}}(z)$ in the layer, an incident vector $\mathbf{k}^0_\rho$, and an *a-priori* RS truncation limit S_R, the polarimetric scattering properties of the layer can be obtained by solving Eq. (30) for two mutually orthogonal linear polarization

states of the incident field, defined here as parallel ($\|$) and perpendicular ($\perp$) to the $\mathbf{k}_\rho^0 - \hat{\mathbf{z}}$ plane. The two transverse components of the scattered plane waves, at propagating RL modes and at each of the two incident polarizations, can then be obtained from Eq. (29) evaluated at $z = 0$ for reflection and $z = H$ for transmission. This leads to an amplitude scattering matrix of the form

$$\begin{pmatrix} A^{\sigma,\mathbf{s}}_{\|\|} & A^{\sigma,\mathbf{s}}_{\|\perp} \\ A^{\sigma,\mathbf{s}}_{\perp\|} & A^{\sigma,\mathbf{s}}_{\perp\perp} \end{pmatrix} = \begin{pmatrix} A^{\sigma}_{F,\|} & 0 \\ 0 & A^{\sigma}_{F,\perp} \end{pmatrix} \delta_{\mathbf{s}} + \begin{pmatrix} \hat{A}^{\sigma,\mathbf{s}}_{\|\|} & \hat{A}^{\sigma,\mathbf{s}}_{\|\perp} \\ \hat{A}^{\sigma,\mathbf{s}}_{\perp\|} & \hat{A}^{\sigma,\mathbf{s}}_{\perp\perp} \end{pmatrix} \tag{32}$$

where $\sigma = +/-$ denotes transmission/reflection, $A^{\sigma}_{F,\|}$ and $A^{\sigma}_{F,\perp}$ are the Fresnel transmission/reflection coefficients for the slab of permittivity $\bar{\epsilon}$ exposed to a plane wave of incidence $\cos\theta^0 = \mathrm{k}^0_{z,0}$, and $\hat{A}$ is the amplitude matrix associated with the source field within the layer

$$\hat{A}^{\sigma,\mathbf{s}}_{\|\,\eta} = \frac{1}{\mathrm{k}^{\mathbf{s}}_{z,0}} \int_0^H dz' \left(\widetilde{G}^{\mathbf{s}}_{x'x'}(z_\sigma, z')\, \widetilde{a}^{\mathbf{s}}_{x',\eta}(z') + \widetilde{G}^{\mathbf{s}}_{x'z}(z_\sigma, z')\, \widetilde{a}^{\mathbf{s}}_{z,\eta}(z') \right) \tag{33}$$

$$\hat{A}^{\sigma,\mathbf{s}}_{\perp\,\eta} = \int_0^H dz' \widetilde{G}^{\mathbf{s}}_{y'y'}(z_\sigma, z')\, \widetilde{a}^{\mathbf{s}}_{y',\eta}(z') \tag{34}$$

with $\widetilde{\mathbf{a}}^{\mathbf{s}}_\eta(z) = R^{\mathbf{s}} \cdot \mathbf{a}^{\mathbf{s}}_\eta(z)$ the rotated source function for incident polarization η and $z_\sigma = 0, H$ for $\sigma = -, +$. The distinction between the homogeneous (i.e., Fresnel) and the inhomogeneous components to Eq. (32) is relevant at the specular reflection and line-of-sight transmission directions corresponding to $\mathbf{s} = (0, 0)$: both components are individually dependent on the fictitious DGF permittivity $\bar{\epsilon}$, yet their sum is independent of $\bar{\epsilon}$. For the free space case ($\bar{\epsilon} = \epsilon_H = 1$) the Fresnel reflection and transmission components would be zero and unity.

The real-valued, 4×4 Stokes scattering matrix $S^{\sigma,\mathbf{s}}_{ii'}$ can be calculated, at each propagating RL direction, from the complex 2×2 amplitude matrix via the usual formulas [3,5]. The S_{11} element, in particular, is given by

$$S^{\sigma,\mathbf{s}}_{11} = \frac{1}{2\mathrm{k}^0_{z,0}} \sum_\eta \sum_{\eta'} \left| A^{\sigma,\mathbf{s}}_{\eta',\eta} \right|^2 \tag{35}$$

This quantity can be interpreted as a bidirectional reflectance/transmittance of the layer, as the intensity scattered into the $\mathbf{s}$ direction, per unit wavelength, would be $S^{\sigma,\mathbf{s}}_{11} I_0(\mathbf{k}^0)$ with I_0 denoting the incident intensity. The hemispherical-directional reflectance and transmittance are obtained from

$$\mathcal{R} = \sum_{\mathbf{s}\ \mathrm{prop}} \mathrm{k}^{\mathbf{s}}_{z,0}\, S^{-,\mathbf{s}}_{11} \tag{36}$$

$$\mathcal{T} = \sum_{\mathbf{s}\ \mathrm{prop}} \mathrm{k}^{\mathbf{s}}_{z,H}\, S^{+,\mathbf{s}}_{11} \tag{37}$$

in which the sum includes all propagating RL modes in region 0 or H.

The divergence of the Stokes vector in the medium, which from energy conservation is equal to the local volumetric absorption rate, is obtained in direct space from the relation $-\mathrm{Im}[\epsilon(\mathbf{r})]|\mathbf{E}(\mathbf{r})|^2$. By using Eqs. (2) and (9) and averaging over the unit cell lateral area, the average differential absorptance of the layer for unpolarized incident radiation is

$$\mathcal{A}'(z) = \mathrm{Im} \sum_\eta \sum_s \left(\mathbf{a}^{\mathbf{s}}_\eta(z) \cdot \mathbf{p}^{\mathbf{s}*}_\eta(z) + \bar{\epsilon} |\mathbf{p}^{\mathbf{s}}(z)|^2 \right) \tag{38}$$

and the total layer absorptance is

$$\mathcal{A} = \int_0^H \mathcal{A}'(z)\, dz \tag{39}$$

Energy conservation would also have

$$\mathcal{A} + \mathcal{R} + \mathcal{T} = 1 \tag{40}$$

This relation can be derived by dotting Eq. (4) with $\mathbf{p}^{\mathbf{s}*}$, employing Green's identities, and integrating over the thickness of the slab. It is strictly valid, however, only in the infinite series sense, i.e., $S_R \to \infty$, and the relative error in satisfying Eq. (40) would need to be checked as part of verifying the calculation results produced by the method.

3. Numerical implementation

3.1. Discretization

The numerical solution of Eq. (30) presents two distinct issues, being 1) the approximation of the integral in Eq. (30), and 2) the evaluation of the Fourier transformed permittivity via Eq. (6). How this latter calculation is performed depends much on the nature of the modeled medium. The present work will focus exclusively on the situation where $\epsilon(\mathbf{r})$ is piecewise constant as opposed to continuous. For this situation the integral over the cell lateral area in Eq. (6) could be reduced to a superposition of integrals over the intersecting particle cross sections. For sufficiently simple particle geometries (spheres, rectangular solids) analytical formulas could be derived for the 2D lateral transform, as a function of z position of the plane relative to the center of the particle. Such an approach would obviously eliminate one source of error from a numerical solution to Eq. (30), yet it would also constrain the method to the simple particle shapes. The approach used here is to compute the Fourier transformed permittivity via numerical means.

As is the case with the standard DD model, the process starts with a 3D analytical representation of the permittivity distribution within the unit cell. The unit cell is then discretized into a 3D array of rectangular solid elements, with each element having a width d_W and height d_H and within which the permittivity is assumed uniform and equal to the value associated with the center of the element. Eq. (6) is approximated using a DFT:

$$\begin{aligned} \widetilde{\epsilon}^{\mathbf{s},j} &= \frac{1}{W^2} \int_{-W/2}^{W/2} dx \int_{-W/2}^{W/2} dy\, e^{-\mathrm{i}\mathbf{k}^{\mathbf{s}}_\rho \cdot \boldsymbol{\rho}}\, \epsilon(\boldsymbol{\rho}, z^j) \\ &\approx \frac{1}{N_W^2} \sum_{\mathbf{i}} \epsilon(\boldsymbol{\rho}^{\mathbf{i}}, z^j) e^{-\mathrm{i}\mathbf{k}^{\mathbf{s}}_\rho \cdot \boldsymbol{\rho}^{\mathbf{i}}} \end{aligned} \tag{41}$$

in which $\mathbf{i} = i_x \hat{\mathbf{x}} + i_y \hat{\mathbf{y}}$, $i_x, i_y = -N_W/2, -N_W/2 + 1 \ldots (N_W - 1)/2$ is a 2D vector index for the lateral position of the element, so that $\boldsymbol{\rho}^{\mathbf{i}} = d_W \mathbf{i}$; $j = 0, 1, \ldots, N_H - 1$ denotes the depth position of the element with $z^j = d_H(j + 1/2)$, and $N_W = W/d_W$, $N_H = H/d_H$ are the number of elements in the horizontal and vertical directions. Eq. (41), which can be efficiently performed using a FFT, sets the maximum wavevector to $\mathrm{k}_{max} \sim \pi/d_W$.

The integral in Eq. (30) has a trivially integratable singularity at $z' = z$ due to the delta function component of the dyadic Green's function. The regular part of the integral is approximated by a midpoint rule, which takes the source function and the DGF to be constant within the element $z^j - d_H/2 \le z \le z^j + d_H/2$:

$$\begin{aligned} &\int_0^H dz'\, \mathbf{G}^{\mathbf{s}}(z^j, z') \cdot \mathbf{a}^{\mathbf{s}}(z') \\ &\approx d_H \left[\sum_{j'=0}^{j} \left(1 - \frac{\delta_{j-j'}}{2} \right) \mathbf{G}^{\mathbf{s}}_{+,reg}(z^j, z^{j'}) \cdot \mathbf{a}^{\mathbf{s},j'} \right. \\ &\quad \left. + \sum_{j'=j}^{N_H-1} \left(1 - \frac{\delta_{j-j'}}{2} \right) \mathbf{G}^{\mathbf{s}}_{-,reg}(z^j, z^{j'}) \cdot \mathbf{a}^{\mathbf{s},j'} \right] \\ &\quad - \frac{1}{\mathrm{m}^2} \hat{\mathbf{z}} \left(\hat{\mathbf{z}} \cdot \mathbf{a}^{\mathbf{s},j} \right) \equiv \sum_{j=0}^{N_H-1} \mathbf{G}^{\mathbf{s},j,j'} \cdot \mathbf{a}^{\mathbf{s},j'} \end{aligned} \tag{42}$$

with $\mathbf{a}^{\mathbf{s},j}$ denoting the source function at z^j. The last term on the right is the contribution due to the delta function, and the term

involving the Kronecker function $\delta_{j-j'}$ is present to avoid counting the $j = j'$ element twice.

The discretized system of equations for the source vector values becomes

$$\mathbf{a}^{\mathbf{s},j} = \hat{\epsilon}^{\,\mathbf{s},j}\Phi^{0,j} + \sum_{\mathbf{s}'} \hat{\epsilon}^{\,\mathbf{s}-\mathbf{s}',j} \sum_{j'=0}^{N_H-1} \mathbf{G}^{\mathbf{s}',j,j'} \cdot \mathbf{a}^{\mathbf{s}',j'} \tag{43}$$

Eq. (43) contains, at most $3N_W^2 N_H$ DOF, being the three vector coefficients of $\mathbf{a}^{\mathbf{s},j}$ for all j and $\mathbf{s}$. The calculations will use a truncated lateral dimension of N_R set by a specified RS unit cell width of k_R, so that $N_R = N_W \mathrm{k}_R/\mathrm{k}_{max}$. Since the permittivity in Eq. (43) can span $2N_R - 1$ values in the lateral directions, a basic criterion for the RS unit cell width would be $\mathrm{k}_R \le \mathrm{k}_{max}/2$; otherwise the permittivity would contain artifacts associated with the periodicity in direct space.

The general appearance of the system of equations is no different than that for a reciprocal space formulation of the DD model for the periodic unit cell geometry. Indeed, the discretized source function $\mathbf{a}^{\mathbf{s},j}$ – which is basically a dimensionless polarization field – is equivalent to the dependent variable in the DD model [1]. It would be possible to manipulate Eq. (43) a bit more to identify a quantity analogous to a polarizability. This would involve separating the part in the sum over j' corresponding to $j' = j$ and bringing it over to the left hand side. The equation could now be multiplied by the inverse of the $\mathbf{a}^{\mathbf{s}',j}$ factor on the left hand side, and would result in a relation in which the source $\mathbf{a}^{\mathbf{s},j}$ was given by a linear relationship between an RS polarizability and the exciting field spectrum at depth j. As is the case with the DD model, this polarizabilty could have weak and strong forms depending on whether the separated part included only the delta function component to the DGF, or the delta function and the regular DGF part for $j = j'$. It would be interesting to see how the RS polarizability so derived was connected to those of the DD model (i.e., Clausius-Mossoti, LDR, etc.) [4,6]. On the other hand, such an analysis is not necessary for the computational model to work, nor would it appear to offer any numerical simplifications or efficiencies to the solution procedure.

3.2. Numerical solution

The biconjugate gradient algorithm is used to solve Eq. (43) for a specified configuration and incident field, and the performance of this method benefits greatly from an optimized algorithm to compute the matrix-vector multiplication in Eq. (43). The DGF is a separable function of z^j and $z^{j'}$ and this allows the $N_H \times N_H$ matrix $\mathbf{G}^{\mathbf{s},j,j'}$, for each $\mathbf{s}$, to be written as a dyadic product of vectors in j and j'; this leads to an $\mathcal{O}(N_H)$ algorithm for performing the matrix multiplication in the z direction. The summation over $\mathbf{s}'$ is performed using the FFT convolution procedure and this requires the permittivity distribution in direct, as opposed to reciprocal, space. The required $(2N_R)^2$ set of permittivity values in DS, needed to perform the convolution of Eq. (43), are obtained by first FFT'ing the original N_W^2 DS values, windowing the $(2N_R)^2$ central values, and inverse FFT'ing back to DS. The convolution in Eq. (43) is now performed by zero–padding $\mathbf{a}^{\mathbf{s},j}$ out to $2N_R$.

A Fortran-90 code, employing the message passing interface (MPI) package, was written to implement the numerical scheme. For a given configuration and incidence direction, the code calculates the 2×2 amplitude and 4×4 Stokes scattering matrices for reflection and transmission at arbitrary directions by 2D spline interpolation of the values at the propagating RL directions. The matrices are based on the PP geometry, in which the incident $(\mathrm{k}_\rho^0 - \hat{\mathbf{z}})$ and scattering $(\mathrm{k}_\rho^{\mathbf{s}} - \hat{\mathbf{z}})$ planes are distinct. When incidence is normal the incident plane becomes arbitrary, and for random medium conditions this allows a numerical averaging of the amplitude and scattering matrices over azimuthal angle, to produce 1D (in polar angle) distributions.

Simulations of random media collect averages of the amplitude and scattering matrices over randomly–sampled configurations. The coherent scattering matrix, again for reflection and transmission, is obtained from the configuration–averaged amplitude matrix. For isotropic random media – which is the case here – the coherent scattering matrix theoretically would be non–zero solely at $\mathbf{s} = (0, 0)$, which corresponds to the specular reflection and line-of-sight transmission directions for a homogeneous slab. This condition is enforced automatically in the simulations, and in this respect any transmission or reflection into directions other than $\mathbf{s} = (0, 0)$ can be interpreted as the diffuse component.

4. Calculation results

4.1. Single particle/particle cluster scattering

The application of the formulation can be broadly split into two categories. The first of these is where the total volume of the particulate matter in the cell is fixed and independent of the cell volume, as would be the case if the cell contains a single or fixed number of particles, and the modeling objective would be to predict the single-scattering (or isolated) properties of the particle or particle cluster. The second case has the particle volume proportional to the cell volume, and the modeling objective becomes the prediction the net scattering effect of a PP layer of the inhomogeneous material represented in the cell. This second category was the original motivation for the work and is the application to which we feel the method has the most potential. Results based on the first category are presented primarily to demonstrate the veracity and identify the limits of the method, as such results can be compared against known benchmarks.

The solution obtained for category 1 is strictly that for plane wave scattering by a 2D infinite square lattice of the particles; each particle, accordingly, is excited by both the plane wave and the secondary (or multiple scattered) component due to the lattice. Unlike the DD superposition model it is not possible to turn the secondary component on or off in the formulation: the periodic behavior is build into the eigenfunction expansion of Eq. (2). And for the same reasons the method, when applied in the category 1 mode, cannot provide a full description of the particle scattered field over 4π steradians; directions along the lateral plane are inaccessible from the solution as this corresponds to the propagation-evanescent boundary in RL space. It would be expected that the error in the predictions, relative to that for true single particle scattering, would increase as scattering directions approach the lattice plane.

Numerical tests were conducted using a spherical particle, with dimensionless radius (i.e., size parameter) of 10 and a refractive index of 1.54. The unit cell width and lateral discretization spacing were fixed at $W = 100$ and $d_W = 0.05$. Incidence is normal, and the directional distributions of reflection and transmission were averaged over azimuth angle. Calculations were performed to examine the roles of two key parameters in the numerical scheme, being the maximum RL maximum wavenumber k_R and the vertical discretization d_H.

Shown in Figs. 1 and 2 are plots of the PWPP scattering matrix element S_{11} and ratios S_{12}/S_{11}, S_{22}/S_{11}, and S_{34}/S_{11} as a function of polar angle, with $\theta < 90$ and > 90 denoting the forward (transmission) and backward (reflection) directions; this quantity is normalized so that

$$\int_0^\pi S_{11}(\theta)|\cos\theta|\,\sin\theta\,d\theta = 1 \tag{44}$$

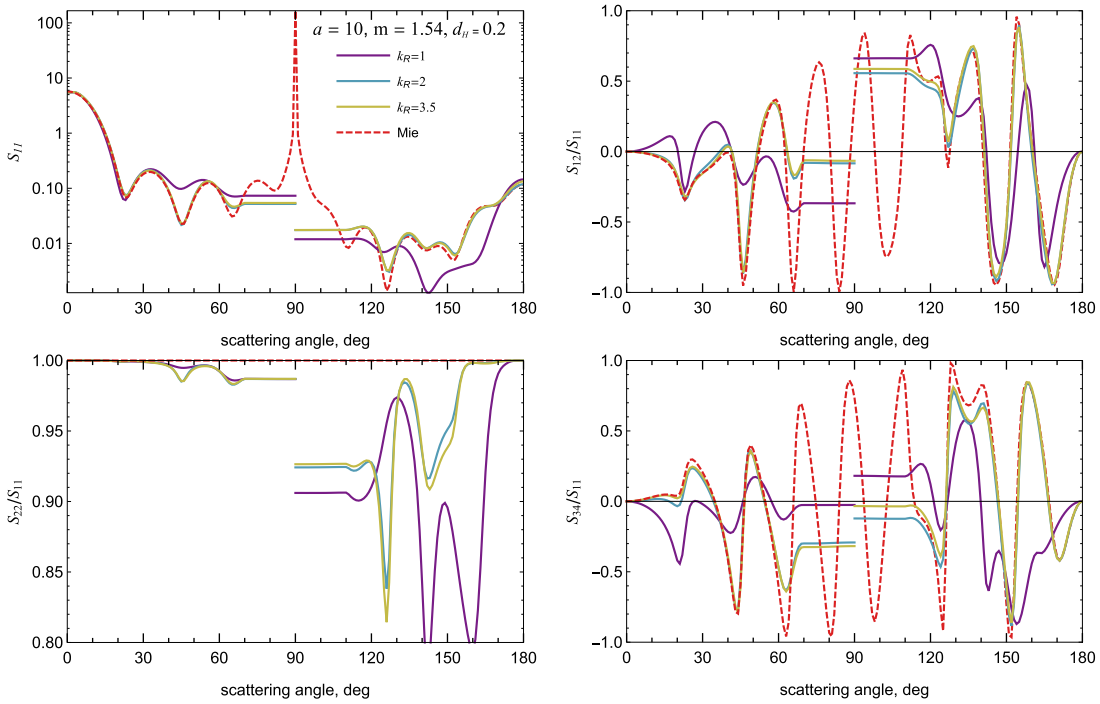

Fig. 1. Distributions of azimuthal–averaged scattering matrix elements for a lattice of widely–separated spheres, as predicted by the PWPP code and approximated by Mie theory. PWPP results are shown for different values of k_R, and $d = 0.2$. Mie results corresponds to $S_{11,\,Mie}/\cos\theta$.

The PWPP results in Fig. 1 have d_H fixed at 0.2 and k_R ranging from 1 to 3.5, and in Fig. 2 $k_R = 2.5$ and d_H ranges from 0.1 to 0.5. As a point of reference, Eq. (43) for the $k_R = 2.5$, $d_H = 0.2$ case contained $3(N_R)^2 N_H = 3(80)^2 108 \sim 2 \times 10^6$ DOF. This is somewhat comparable to the DOF of a $d = 0.2$ DD system applied to the $a = 10$ sphere, although this equivalence is mostly by coincidence; keeping the same k_R, W, and d_H, and halving the sphere radius, would only reduce the PWPP DOF by half. A value of $\overline{m} = 1$ (i.e., the free space form) minimized the number of iterations required for solution, which is expected as the volume-averaged permittivity of the unit cell is close to unity. What is interesting about the calculations is that, with the sole exception of the $k_R = 1$ case, the number of iterations required to reach a fixed error residual remained fairly constant (at around 300) for the different values of k_R and d_H; the $k_R = 1$ case required about half this value. Included is the Mie theory result; the appropriate quantity for comparison with PWPP is $S_{11,\,Mie}(\theta)/|\cos\theta|$, where $S_{11,\,Mie}$ is the Mie scattering phase function.

The results in Figs. 1 and 2 generally show that, given a sufficient large k_R and sufficiently small d_H, and considering scattering angles not too close to 90°, the PWPP model can reproduce to good accuracy the polarimetric scattering features predicted by Mie theory. The results for the largest k_R in Fig. 1, and the smallest d_H in Fig. 2 are, for all practical purposes, converged in their respective parameter, and the direction of convergence is generally towards the Mie predictions. On the other hand, a limited set of additional calculations indicated that, for the set unit cell width of 100, the difference between the PWPP and Mie predictions cannot be made arbitrary small through use of a sufficiently large k_R *and* a sufficient small d_H; this is especially evident in the depolarization ratio S_{22}/S_{11} which, for the sphere, is exactly unity.

Using the same single-sphere configuration, a set of calculations was performed to examine the effect of the unit cell width W on the predictions; results are shown in Fig. 3 and correspond to $k_R = 2.5$ and $d_H = 0.2$. The solid lines in the plots represent the mean S_{11} and S_{12}/S_{11} as calculated from nine values of W ranging from 100 to 150, and the shaded area around each line corresponds to $\pm$ one standard deviation from the mean as calculated from the nine samples. It can be seen that W has the largest sensitivity on the results in generally the same θ regions as those with the largest discrepancy with the exact (Mie) results. Overall, however, the effect of W does not appear to be significant, especially in the near–forward and backward directions.

Additional tests were performed with cells containing multiple spheres placed at fixed locations within the cell, and benchmark calculations were calculated using the MSTM code [7]. These tests are useful as they can examine how the model captures the interaction effects between different scatterers. Fig. 4 shows the reflection/transmission distribution in the $x-z$ plane as calculated for a system of three identical spheres spaced equidistantly along the x axis, with sphere separation distance as a parameter. The spheres have $a = 2$ and $m = 1.54$, incidence is normal to the plane, and computations were performed using $W = 100$, $d_W = 0.05$, $d_H = 0.2$, and $k_R = 2.5$. The PWPP predictions have been scaled so that they agree with MSTM at $\theta = 0$. Increasing separation results in an increasingly complex interference pattern, as expected. The PWPP model can capture the relatively broad lobes in this pattern at angles less than around 70° or greater than 110°, yet the details of the narrow features, which become increasing prominent for large separation, are missed. This behavior is even more evident in Fig. 5, which shows the linear polarization ratio S_{12}/S_{11} in the $x-z$ plane for the same system and as predicted by PWPP and MSTM; at the largest separation of $x_1 - x_2 = 40$ – for which the 3-sphere cluster is practically spanning the entire unit cell – the PWPP predictions appear somewhat like a crude, low-pass filtering of the exact MSTM results.

The PWPP and MSTM predictions for the 3 sphere system come into better agreement when the scattered distribution is averaged over azimuth angle; for the normal incident conditions of the tests the azimuth–averaged distribution would be equivalent to that produced by the 3-sphere chain randomly oriented in the lateral plane. Results of this averaging, for the $x_1 - x_2 = 40$ case, are

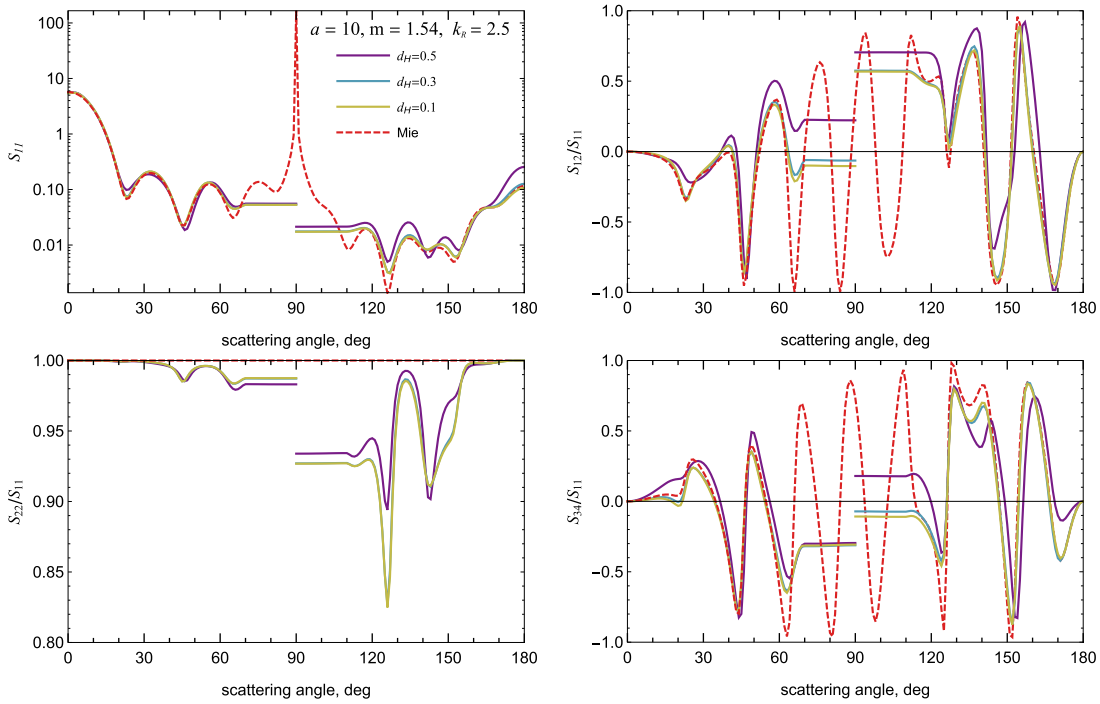

Fig. 2. Distributions of azimuthal–averaged scattering matrix elements for a lattice of widely–separated spheres, as predicted by the PWPP code and approximated by Mie theory. Transmission and reflection correspond to $\theta < 90°$ and $> 90°$. PWPP results are shown for different values of discretization spacing d_H, and $k_R = 2.5$.

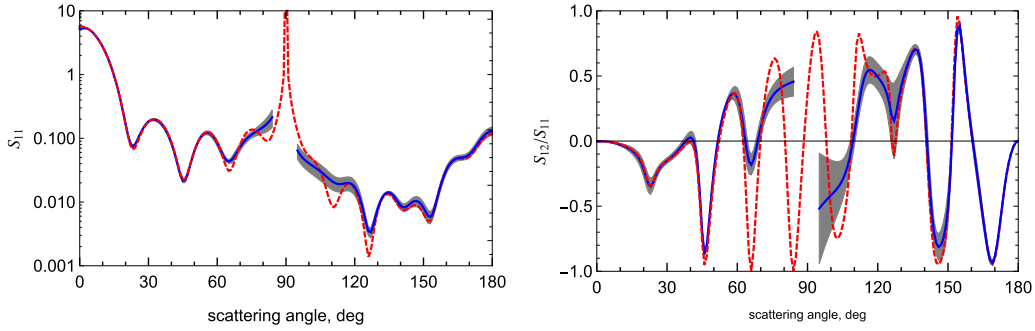

Fig. 3. Effect of unit cell width on azimuthal–averaged S_{11} and S_{12}/S_{11} for the single sphere of Fig. 2. Solid lines are mean values calculated using W ranging from 100 to 150, and shaded areas denote the $\pm$ one standard deviation spread. Dashed line is the exact Mie result.

shown in Fig. 6. Orientation averaging acts to erase the sharp features produced by interference, and reveals patterns that are more associated with the individual particles and the near–field coupling among them. The MSTM polarization ratio in Fig. 6, in particular, is only slightly different than that produced by a single, isolated sphere; this is expected due to the relatively large separation distance between the spheres.

Several similar tests using various combinations of spheres were performed, and all supported the basic conclusions discussed above. In particular, the PWPP method, when applied to single particles or particle clusters, can predict with reasonable accuracy the broad features of polarimetric scattering at directions sufficiently removed from those tangent to the lateral plane. The accuracy increases when the properties are averaged over different orientations or configurations of the particle clusters.

4.2. Random media

Having established some confidence in the method from the category-1 calculations, attention is now turned to situations in which the unit cell contains a representative sample of a discretely random medium. To do this, the simple Monte Carlo algorithm described in [1] is used to generate particle coordinate sets as a function of the specified volume fraction of particulate media, the distributions functions of size, shape, orientation, and composition, and the unit cell W and H. The $z = 0$ and H boundaries are defined as the minimum and maximum extent of the particulate material, and the particles are not sliced at the boundaries (i.e., all particles are intact); because of this, the lateral area-averaged particulate volume fraction of the cell transitions from zero, at the boundaries, to the infinite–medium value set in the sampling algorithm, over a distance of around two particle radii from the boundaries.

Unlike that for the category 1 calculations, the DGF permittivity $\bar{\epsilon}$ can have a significant impact on the convergence rate of the iterated solution for random media simulations. Basically, the effect of $\bar{\epsilon}$ is equivalent to an analytical preconditioning of Eq. (43). An argument for this starts with the observation that the electric field vector $\mathbf{p}^s(z)$ in Eq. (29) is not a function of $\bar{\epsilon}$, yet the incident field and source field vectors are. And since the condition number of Eq. (43) will be a function of $\bar{\epsilon}$, among other things, it follows that, all other things constant, there should be some optimum value of $\bar{\epsilon}$ which minimizes the condition number and thus

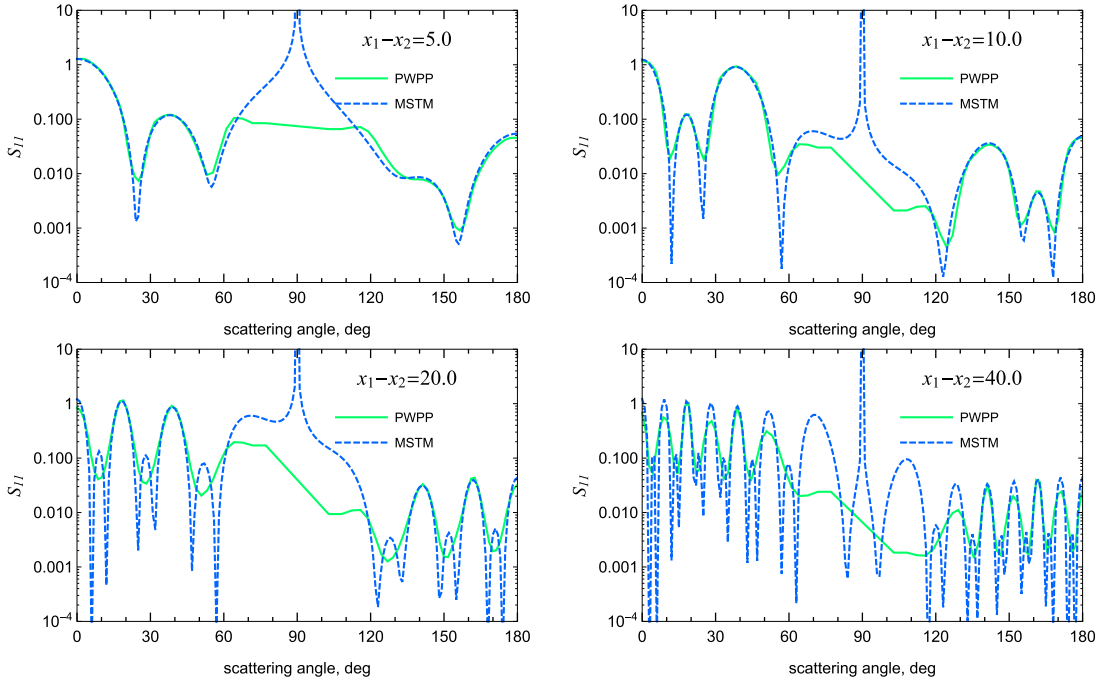

Fig. 4. Plots of normalized intensity in the $x-z$ plane as predicted by PWPP and MSTM theory, for a system of 3 spheres lying on the x axis, with $a = 2$, $m = 1.54$, and as a function of dimensionless center-to-center distance $x_2 - x_1$. Incidence is normal.

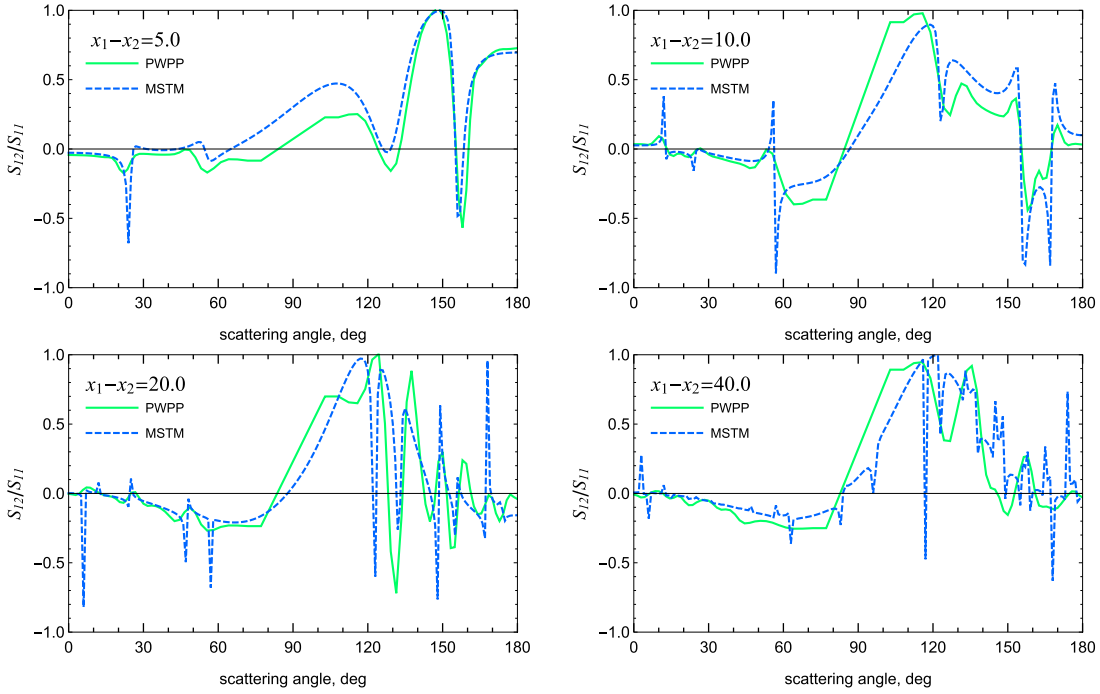

Fig. 5. Plots of linear polarization ratio S_{12}/S_{11} $x-z$ plane as predicted by PWPP and MSTM theory. System is the same as in Fig. 4.

optimizes the iterative solution of Eq. (43). Put another way, the formulation developed here is a form of invariant imbedding: the actual, inhomogeneous unit cell is modeled as the superposition of a fictitious homogeneous unit cell and a "shifted" inhomogeneous unit cell, and the only part of this superposition that requires numerical attention is that for the shifted cell.

Of course, knowing the value of $\overline{\epsilon}$ which minimizes the condition number is another problem altogether. One indication of the value can be obtained by averaging Eq. (29), written for $\mathbf{s} = (0, 0)$, over randomly sampled configurations:

$$\langle \mathbf{p}^0(z) \rangle - \Phi^0(z;\overline{\epsilon}) = \int_0^H dz' \, \mathbf{G}^0(z,z';\overline{\epsilon}) \cdot \langle \mathbf{a}^0(z';\overline{\epsilon}) \rangle \tag{45}$$

in which $\langle \ldots \rangle$ denotes averaging over configuration. The quantity $< \mathbf{p}^0(z) >$ is, by definition, the coherent field, and is (again) independent of $\overline{\epsilon}$. Effective medium theory would set $\langle \mathbf{p}^0(z) \rangle = \Phi^0(z;\epsilon_c)$, where ϵ_c is the effective permittivity of the medium; the imaginary part of this quantity, which will be > 0 for any sit-

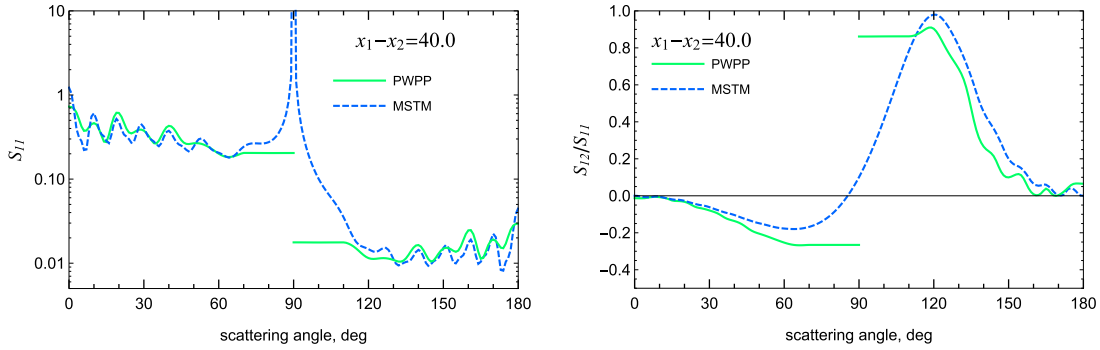

Fig. 6. Plots of azimuth-averaged intensity and linear polarization, as predicted by PWPP and MSTM, for the conditions of Fig. 4 and with $x_1 - x_2 = 40$.

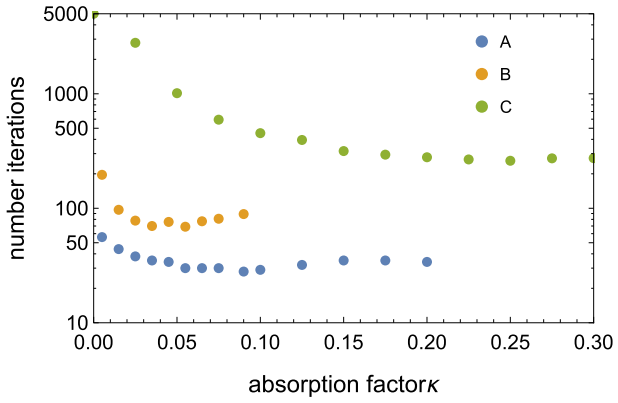

Fig. 7. Effect of absorption factor κ in Eq. (46) on iteration count, for three conditions identified in text.

uation of relevance here, describes the extinction of the coherent field due to the combined effects of absorption and scattering, and as a consequence the coherent field will exponentially decay with z. When $\overline{\epsilon} = 1$ (the FS DGF) the magnitude of the incident field $\Phi^0(z;\ 1)$ will be order-unity and constant. Consequently, for this case the integral on the right hand side must cancel both the coherent and the incident fields at any depth z, and this implies that the source function will have the same exponential decay as the coherent field. This basic principle forms a foundation of effective medium theory, and it is implemented by splitting the integral into parts dependent on the boundary at $z' \to 0$, which cancels the incident field, and $z' \to z$, which cancels the coherent field [8,9].

Consider now what happens when $\overline{\epsilon} = \epsilon_c$. The integral in Eq. (45) will, hypothetically, be zero, and this implies $\langle \mathbf{a}^0(z;\overline{\epsilon})\rangle = 0$. In particular, the source function no longer has to cancel the incident field, as this is now done by the coherent field. We suspect that this would minimize the condition number of the matrix representing Eq. (43), as the eigenvalues of this matrix would be connected to the exponential coefficients that describe the variation of $\mathbf{a}^{\mathbf{s}}$ with z. A more rigorous examination of this issue is left to those with more mathematical skills.

In regards to numerical computations, $\overline{\epsilon} = \epsilon_c$ is not an especially practical choice simply because ϵ_c is not known *a-priori*. The approach taken here is to set

$$\overline{\epsilon} = \epsilon_m + \mathrm{i}\,\kappa \tag{46}$$

where ϵ_m is the volume-averaged permittivity of the entire cell and κ is a positive and real absorption factor. The effect of κ on solution convergence is illustrated in Fig. 7, which shows the iteration count needed to reach a relative residual error of 10^{-6}, as a function of κ. The medium consists of a single configuration of $a = 4$ spheres randomly dispersed in an $H = 20$ layer with a volume fraction of 0.2, with $W = 100$, $d_W = 0.05$, $d_H = 0.2$, and $\mathrm{k}_R = 2.5$. Three results are shown corresponding to different values of the particle and background medium refractive index, with (A) $\mathrm{m}_P = 1.54 + 0.1\mathrm{i}$, $\mathrm{m}_B = 1$; (B) $\mathrm{m}_P = 1.31$, $\mathrm{m}_B = 1$; and (C) $\mathrm{m}_P = 2.7$, $\mathrm{m}_B = 1.54 + 0.01\mathrm{i}$. The background material, for these calculations, is the medium between 0 and H not occupied by spheres, and $\epsilon_H = 1$ for all cases. For each case increasing κ from zero significantly reduces the iteration count to a point where it is minimized or becomes flat. This effect is even more relevant when compared against the iteration count for the $\overline{\epsilon} = 1$ case, which for A and B was 197 and 530; for C the problem had not converged after 5000 iterations and had no indication of ever converging. The A and B cases had an optimum κ that was relatively close to 1/2 times the RT extinction coefficient, i.e.,

$$\kappa \approx \frac{3 f_v Q_{ext}}{8\pi a} \tag{47}$$

where Q_{ext} is the Mie extinction efficiency and f_v the sphere volume fraction. It would be expected that this relation would work for the C case as well, although the absorbing background medium makes somewhat non-trivial the calculation of the RT extinction coefficient for the medium.

An illustration of what the PWPP method actually predicts when applied to random media is presented in Fig. 8. Shown are the scattering matrix elements for a system of $N_P = 321$ spheres, with $a = 2$ and $\mathrm{m} = 1.31$, randomly distributed in the unit cell. The background is vacuum. Constant model parameters are $d_W = 0.05$, $d_H = 0.2$, $W = 100$, and $\mathrm{k}_R = 2.5$. This particular set of particle parameters corresponds to an RT optical thickness (extinction coefficient · layer thickness) of 0.25. The layer thickness is the variable parameter in the PWPP curves, with $H = 7.5$, 15, 30, and 60; this corresponds to average unit cell volume fractions of 0.144, 0.0721, 0.0362, 0.0179. Incidence is normal, and the results are averaged over azimuthal angle and over 600 randomly sampled configurations of the unit cell. Appearing also as the dotted line are the vector RTE results, as calculated by Mie theory and the adding-doubling algorithm.

The DGF permittivity was calculated using (47), and the range of iteration count for all four cases was 35–50 and independent of the volume fraction; the effect of the $\overline{\epsilon}$ preconditioning was most significant (over a factor of 10 improvement over the free space case) at the highest volume fractions. All results under-predicted energy conservation in Eq. (40), resulting in an apparent absorptance for the physically non absorbing layer; the maximum was 0.011 and occurred at the largest layer thickness.

The S_{11} curves, which are normalized per Eq. (44), describe the relative distribution of scattered energy. Fig. 8 shows that increasing packing density (smaller H) shifts the distribution towards the backward, i.e., reflection, directions. The total scattered power, it turns out, actually decreases with increasing f_v for this particular

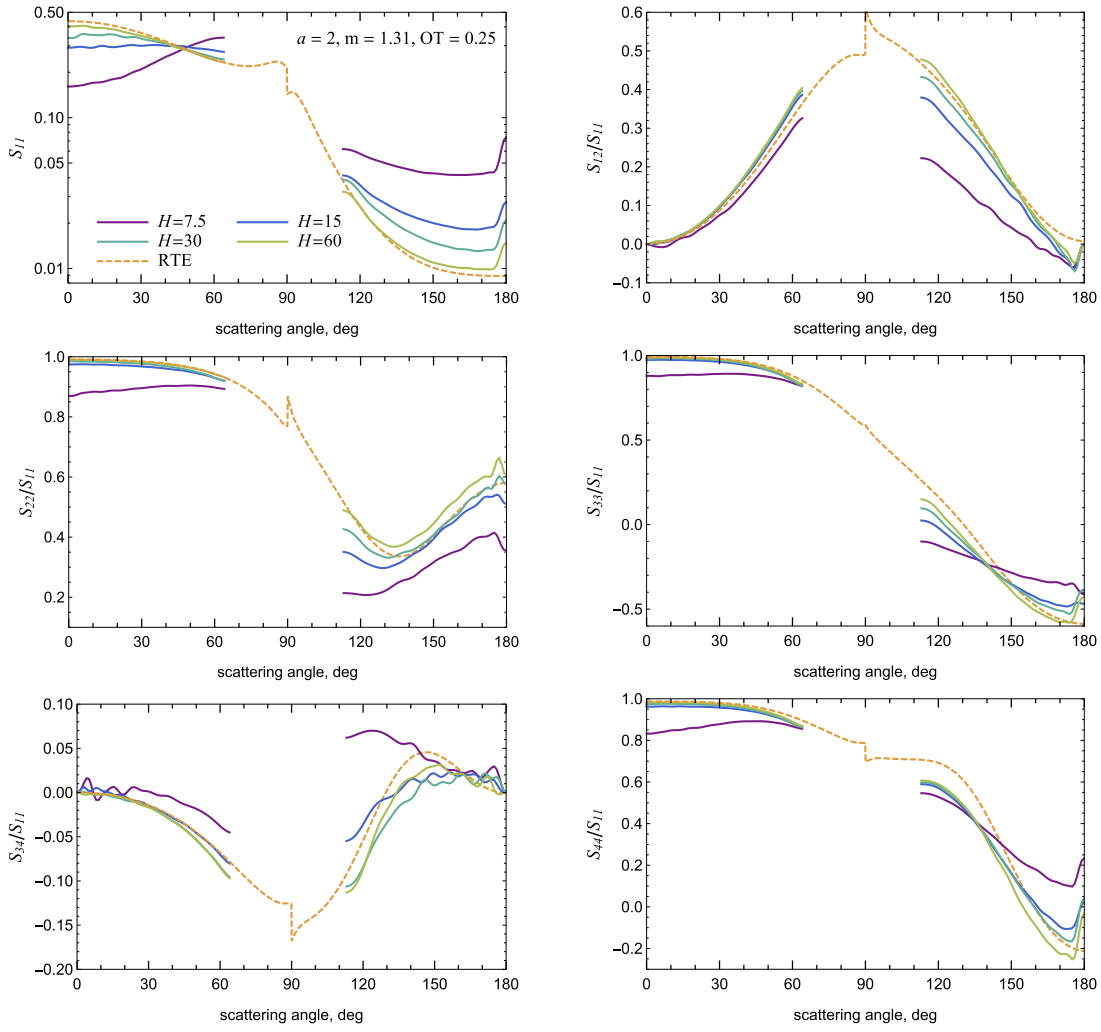

Fig. 8. Distributions of azimuthal–averaged scattering matrix elements for a system of $N_P = 321$ spheres, with $a = 2$, $\mathrm{m} = 1.31$, randomly dispersed in a $W = 100$ unit cell, as calculated by PWPP for different cell thicknesses H. Also shown are the VRTE results.

case; this is consistent with our previous results using the MSTM code [10]. Also consistent with previous investigations is that the direct solution results converge to those of the RT as f_v becomes small – with the important exception of the backwards direction.

The polarimetric ratios follow the same basic trend: increasing f_v shifts the ratios towards the direction of increasing RT optical thickness and the effect is most significant in the backwards hemisphere. The discrepancy between the PWPP results, at the smallest f_v, and RT are also greatest in this hemisphere: PWPP curves appear to uniformly under or overshoot the RT limit.

The PWPP results show features characteristic of coherent backscattering and polarization opposition. At the highest f_v, $S_{11}(180^\circ)/S_{11}(165^\circ) = 1.77$, which is consistent with direct simulation calculations using the superposition T matrix method for spherical clusters of spherical particles [11]. The same report, however, shows a much more pronounced suppression of the CB peak with decreasing f_v. The same trend is true for the polarization opposition effect in S_{12}/S_{11}. The depolarization ratio S_{22}/S_{11}, on the other hand, shows behavior at high f_v, i.e., the formation of a negative peak, that has not been observed (to our knowledge) in other direct simulation experiments.

We do not think that the results in Fig. 8 should be overinterpreted or generalized: this is the initial shakedown cruise of the method and more benchmarking is needed to assess sources of error and their remedy. In particular, the width of the CB/PO effects are similar to the angular resolution $2\pi/W$ used in the experiments, and the current calculations are incapable of observing the narrowing of the peaks with decreasing f_v. Normal incidence conditions also superimpose the CB effects with the "real" coherent effect, i.e., specular reflection, and it is difficult to know for sure if one has been isolated from the other. Nevertheless, the results are entirely encouraging and much better than we expected going into this project.

5. Summary

A key distinction of the present model with those traditionally used in scattering (DDA, T matrix, FDTD) is how the medium is represented. The fundamental information characterizing the medium in Eq. (30) is the depth–dependent truncated lateral Fourier spectrum of the permittivity. In the applications examined here this spectrum was calculated by DFTing and windowing a direct space distribution, but this is not especially salient to the basic functionality of Eq. (30). The important point is that any distribution of particle sizes, shapes, compositions, and/or concentrations that gave the same permittivity distribution in **s** and z *would have the same* far–field polarimetric scattering properties.

A second distinction is the fundamental, or primitive, mathematical representation of the vector EM field. The basic element in the present model is the plane wave, and, accordingly, the model

automatically reduces to Fresnel theory for homogeneous layers. Indeed, the basic solution algorithm could have application to the calculation of thin layered films [12].

The numerical model developed was built primarily to test the theory in the easiest way possible; no doubt there are many ways that the algorithm could be made more efficient and involve fewer DOF. The fact that it does not automatically satisfy energy conservation at arbitrary truncation is a flaw that perhaps could be remedied by a patch in the permittivity spectrum or the DGF. An additional issue/limitation is the use of brute force, Monte Carlo methods to generate useful and reliable averages for random medium modeling. This would be especially pertinent for calculations with oblique incidence, as the speckle now must be averaged out over two directional variables. Monte Carlo is very simple and efficient on parallel networks, and big computing may simply obviate this issue in the near future. But there would be interesting and challenging mathematical extensions to the formulation that could produce something analogous to the analytical orientation averaging possible with T matrix models. In particular, the periodic model could be extended to the z direction, leading to a Bloch theorem formulation analogous to those applied to scattering (EM, electron, phonon) by crystal lattices [13,14]. This would basically be an effective medium theory, built upon the Fourier representation of the unit cell in three dimensions.

In closing, the lead author would like to note that the basic idea for the present work was conceived after the formulas, and code, for the plane parallel DD model in [1] had been put together and applied in several computational runs. He wishes that he had thought of it before. Perhaps some fatal flaw or serious limitation will be found that limits the model to special conditions, such as soft material or simple particle shapes. As of now, however, the PWPP model appears to be able to do everything the DD model can, with comparable or better computational size and speed and a vastly simpler formulation and code.

Appendix

List of acronyms

DD	discrete dipole	ODE	ordinary differential equation
DDA	discrete dipole approximation	PDE	partial differential equation
DFT	discrete Fourier transform	PP	plane parallel
DGF	dyadic Green's function	RL	reciprocal lattice
DOF	degrees of freedom	RS	reciprocal space
DS	direct space	RT	radiative transport
FFT	fast Fourier transform	VIE	volume integral equation
EM	electromagnetic		

Incident field

In rotated coordinates, the rotated components of the incident field vector amplitude appears as

$$\hat{\mathbf{x}}\cdot\Phi^0(z;\overline{\epsilon}) = \frac{2\overline{\mathrm{m}}\,\mathrm{m}_0\mathrm{k}_z^0\mathrm{k}_{z,0}^0}{D_\parallel^0}\Big(\mathrm{i}\,\overline{\mathrm{m}}\,\mathrm{k}_{z,H}^0\cos(\overline{\mathrm{m}}\,\mathrm{k}_z^0(H-z)) + \mathrm{m}_H\,\mathrm{k}_z^0\sin(\overline{\mathrm{m}}\,\mathrm{k}_z^0(H-z))\Big) \tag{48}$$

$$\hat{\mathbf{y}}\cdot\Phi^0(z;\overline{\epsilon}) = -\frac{2\overline{\mathrm{m}}\,\mathrm{m}_0\mathrm{k}_z^0\mathrm{k}_{z,0}^0}{D_\perp^0}\Big(\mathrm{i}\,\overline{\mathrm{m}}\,\mathrm{k}_z^0\cos(\overline{\mathrm{m}}\,\mathrm{k}_z^0(H-z)) + \mathrm{m}_H\,\mathrm{k}_{z,H}^0\sin(\overline{\mathrm{m}}\,\mathrm{k}_z^0(H-z))\Big) \tag{49}$$

$$\hat{\mathbf{z}}\cdot\Phi^0(z;\overline{\epsilon}) = -\frac{2\overline{\mathrm{m}}\,\mathrm{m}_0\sqrt{1-\mathrm{k}_z^{02}}\,\mathrm{k}_{z,0}^0}{D_\parallel^0}\Big(\mathrm{i}\,\mathrm{m}_H\,\mathrm{k}_z^0\cos(\overline{\mathrm{m}}\,\mathrm{k}_z^0(H-z)) + \mathrm{m}\,\mathrm{k}_{z,H}^0\sin(\overline{\mathrm{m}}\,\mathrm{k}_z^0(H-z))\Big) \tag{50}$$

References

[1] Mackowski DW. Van de Hulst Essay: the dda, the rte, and the computation of scattering by plane parallel layers of particles. J Quant Spectrosc Radiat Transfer 2017;189:43–59.

[2] Draine B, Flatau P. Discrete-dipole approximation for periodic targets: theory and tests. JOSA A 2008;25(11):2693–703.

[3] Hovenier JW, van der Mee CV, Domke H. Transfer of polarized light in planetary atmospheres: basic concepts and practical methods, V. 318. Springer Science & Business Media; 2014.

[4] Lakhtakia A, Mulholland GW. On two numerical techniques for light scattering by dielectric agglomerated structures. J Res Natl Inst Stand Technol 1993;6:699–716.

[5] Bohren CF, Huffman DR. Absorption and scattering of light by small particles. Wiley; 1983.

[6] Yurkin MA, Hoekstra AG. The discrete dipole approximation: an overview and recent developments. J Quant Spectrosc Radiat Transfer 2007;106:558–89. doi:10.1016/j.jqsrt.2007.01.034.

[7] Mackowski DW, Mishchenko MI. A multiple sphere T-matrix fortran code for use on parallel computer clusters. J Quant Spectrosc Radiat Transfer 2011;112:2182–92.

[8] Bringi VN, Varadan VV, Varadan VK. Coherent wave attenuation by a random distribution of particles. Radio Sci 1982;17:946–52.

[9] Ishimaru A, Kuga Y. Attenuation constant of a coherent field in a dense distribution of particles. J Opt Soc Amer A 1982;72(10):1317–20.

[10] Ramezanpour B, Mackowski DW. Comparison of radiative transport and dda prediction of polarized reflectance and transmittance from random particulate layers. J Quant Spectrosc Radiat Transfer, Submitted for publication.

[11] Dlugach JM, Mishchenko MI, Liu L, Mackowski DW. Numerically exact computer simulations of light scattering by densely packed, random particulate media. J Quant Spectrosc Radiat Transfer 2011;112:2068–78.

[12] Zhang ZM. Nano/microscale heat transfer. New York, NY: McGraw-Hill; 2007.

[13] Lamb W, Wood D, Ashcroft N. Long-wavelength electromagnetic propagation in heterogeneous media. Phys Rev B 1980;21(6):2248.

[14] Stefanou N, Karathanos V, Modinos A. Scattering of electromagnetic waves by periodic structures. J Phys 1992;4(36):7389. http://stacks.iop.org/0953-8984/4/i=36/a=013.